Geotextiles and Geomembranes 46 (2018) 685–698

Contents lists available at ScienceDirect

Geotextiles and Geomembranes

journal homepage: www.elsevier.com/locate/geotexmem

Effect of particle shape on the response of geogrid-reinforced systems: Insights from 3D discrete element analysis☆

Ge Gao[a], M.A. Meguid[b,*]

[a] Civil Engineering and Applied Mechanics, McGill University, 817 Sherbrooke St. W, Montreal, Quebec, H3A 0C3, Canada
[b] Civil Engineering and Applied Mechanics, McGill University, 817 Sherbrooke St. W, Montreal, QC, H2A 0C3, Canada

ARTICLE INFO

Keywords:
Geosynthetics
Geogrid-reinforced foundation
Discrete element
Particle shape
Triaxial test
Bearing capacity

ABSTRACT

Understanding soil-geogrid interaction is essential for the analysis and design of reinforced soil systems. Modeling this interaction requires proper consideration for the geogrid geometry and the particulate nature of the backfill soil. This is particularly true when angular soil particles (e.g. crushed limestone) are used as a backfill material. In this study, a three-dimensional (3D) discrete element model that is capable of capturing the response of unconfined and soil-confined geogrid material is developed and used to study the response of crushed limestone reinforced with geogrid and subjected to surface loading. The 3D shape of the crushed limestone is modeled by tracing the surface areas of a typical particle and fitting a number of bonded spheres into the generated surface. Model calibration is performed using triaxial tests to determine the microparameters that allow for the stress-strain behaviour of the backfill material to be replicated. To demonstrate the role of particle shape on the soil-geogrid interaction, the analysis is also performed using spherical particles and the calculated response is compared with that obtained using modeled surfaces. The biaxial geogrid used in this study is also modeled using the discrete element method and the unconfined response is compared with the available index test results. This study suggests that modeling the 3D geogrid geometry is important to accurately capture the geogrid response under both confined and unconfined conditions. Accounting for the particle shape in the analysis can significantly enhance the predicted response of the geogrid-soil system. The modeling approach proposed in this study can be adapted for other reinforced soil applications.

1. Introduction

Geogrid has been successfully used for the reinforcement of different geotechnical structures (e.g. railway tracks, road embankments, foundations and retaining walls). The reinforcing effects generally develop via the interaction between the reinforcing material and the surrounding soil. This interaction can be very complex depending on the nature and properties of the reinforcement material and the interlocking effect that may develop due to the partial penetration of particles through the geogrid apertures.

A large number of laboratory tests and theoretical studies have been used over the past three decades to investigate the interaction mechanism between geogrid and the surrounding soil (e.g. Palmeira and Milligan, 1989; Moraci and Recalcati, 2006; Shin and Das, 2000; Sitharam and Sireesh, 2004; Demir et al., 2013; Lin et al., 2013; Ezzein and Bathurst, 2014; Bathurst and Ezzein, 2015, 2016; 2017; Cardile et al., 2017; Esmaeili et al., 2017; Mousavi et al., 2017; Saha Roy and Deb, 2017). Numerical analysis using finite element (FE) has been also used to predict the failure load as well as the displacements and strains developing in the reinforcement (Ling and Liu, 2009; Li et al., 2012; Kumar and Sahoo, 2013; Rowe and Liu, 2015; Hussein and Meguid, 2016; Zhuang and Wang, 2016). One inherent limitation of these methods is the difficulty in analyzing the soil-geogrid interaction at the particle level.

The discrete element method (DEM) (Cundall and Strack, 1979), has a particular advantage in capturing the kinematic behaviour of discontinuous media at the microscopic level (Stahl and Konietzky, 2011; Wang et al., 2016; Jiang et al., 2016; Shen et al., 2017; Gao and Meguid, 2018a; Lai and Chen, 2017). The method has also been used to investigate the interface behaviour of geogrid-soil system considering the discontinuous nature of granular particles. Ngo et al. (2017) studied the interface behaviour of geogrid-reinforced subballast through a series of large-scale direct shear tests and discrete element analysis. It was found that shear strength of the interface is governed by the geogrid characteristics, including geometry and opening size. Chen et al. (2014) evaluated the interlocking behaviour of geogrid-reinforced

☆ A preprint submitted to Geotextiles and Geomembranes December 19, 2017.

* Corresponding author.
E-mail addresses: ge.gao2@mail.mcgill.ca (G. Gao), mohamed.meguid@mcgill.ca (M.A. Meguid).

https://doi.org/10.1016/j.geotexmem.2018.07.001
Received 20 December 2017; Received in revised form 7 April 2018; Accepted 2 July 2018

railway ballast using discrete element method and found that modeling ballast particles as clumps holds much promise for investigating the interaction between geogrids and ballast material. Lai et al. (2014) investigated geogrid-reinforced pile-supported embankment using DEM and found that soil arching is a key factor in the load transfer mechanism from the embankment to the foundation system, which is strongly affected by the presence of the geogrid reinforcement. Chen et al. (2012) studied the cyclic loading of geogrid-reinforced ballast under confined and unconfined conditions, and concluded that geogrid reinforcement can significantly limit the lateral displacement in the reinforced zone. The above studies demonstrated that the stress-strain behaviour of a geogrid material embedded in backfill soil is complex, particularly for angular soil particles of irregular shapes as they interact with one or more geogrid layers.

The objective of this study is to propose a 3D particulate model that is able to capture the response of both unconfined and soil confined biaxial geogrid embedded in crushed rock material and subjected to surface loading. This is achieved in three phases as follows:

i) Modeling crushed limestone: The shape of a typical particle is simulated based on crushed limestone material used in laboratory experiments. The input parameters needed for the discrete element analysis are determined using triaxial and direct shear tests.
ii) Developing particle-based geogrid model: A 3D geogrid model is created using parallel bond between particles. The model is validated using tensile and flexural test results to ensure that the response of the geogrid material is properly captured under the applied loading.
iii) Analyzing a case study: Using the created backfill and geogrid models, a case study involving a square footing over geogrid-reinforced soil is analyzed and the results are compared with experimental data.

The analysis presented in this study has been performed using the particle flow code (PFC^{3D}), version 5.0 (Itasca, 2014).

2. Modeling crushed limestone

Particle shape is known to influence the inter-particle friction, contact forces and coordination number. Researchers (e.g. Stahl and Konietzky, 2011; Chen et al., 2012; Stahl et al., 2014; Indraratna et al., 2014; Miao et al., 2017) have used clump logic in modeling complex-shaped particles in various applications. A clump is defined as a single rigid body of overlapping spherical pebbles of different sizes that acts as a single particle of a chosen or arbitrary shape (Gao and Meguid, 2018a; 2018b). In this study, an approach has been developed to create irregular shaped particles based on the construction of a triangular mesh that traces the actual geometry of a typical crushed limestone particle (Fig. 1). For the purpose of this investigation, crushed limestone material is selected based on the reported laboratory experiments performed by Chen et al. (2009). To demonstrate the effect of particle shape on the response of geogrid embedded in crushed limestone, the analysis is also performed using spherical particles and the response is compared with that obtained using irregular shaped clumps.

2.1. Triaxial compression tests

Several researchers used discrete element analysis to study soil-geogrid interaction (e.g. Lai et al., 2014; Wang et al., 2016; Miao et al., 2017; Ngo et al., 2017), however, only a limited number of these studies fully calibrated the set of microparameters that govern both the interface and interlocking effects, including the effective modulus, stiffness ratio (normal to shear stiffness ratio), peak and residual friction coefficients.

In this study, large-scale triaxial tests are used to determine the effective modulus of the contact that is needed for the discrete element

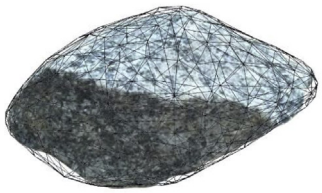

(a) Triangular mesh that traces the shape of a typical particle

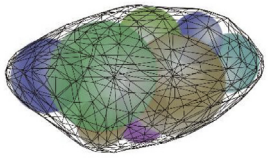

(b) Fitting spheres inside the mesh to create particle-shaped clump

Fig. 1. Modeling crushed limestone particles: (a) Triangular mesh that traces the shape of a typical particle; (b) Fitting spheres inside the mesh to create particle-shaped clump.

analysis. The linear-based model depicted in Fig. 2 is used to represent the contacts between particles as well as between particles and rigid boundaries. A cylindrical sample 200 mm in diameter and 500 mm in height is modeled as shown in Fig. 3. A servo-mechanism is simulated and used to apply the confining pressures acting on the samples in both axial and radial directions. Careful consideration is usually given to particle size such that a reasonable balance between the computational cost and scaling effect is maintained (Tran et al., 2014b). In this study, spheres that represent particles of average diameter of 5.67 mm were initially generated using a scale factor of 3 (ratio of numerically generated to actual particle size), thus the diameter of the spherical particle is approximately 17 mm. The particle assembly is then cycled to equilibrium, which is considered to be reached when the ratio of unbalanced forces to the mean contact forces are smaller than a set tolerance value of 10^{-5} (Masson and Martinez, 2001). The modeled spheres were then replaced by the irregular shaped clumps that have been previously created to capture the geometry of a typical crushed limestone particle. The system is again cycled to equilibrium to reduce the excess contact forces resulting from the random placement of the clumps (Lu and Mcdowell, 2006; Chen and McDowell, 2013).

Stahl and Konietzky (2011) demonstrated that modeling the loading-unloading phase of the triaxial tests allows for the deformability of the system to be determined with a reasonable accuracy. Therefore, the response of the particles under loading-unloading condition is simulated in this study at an average confinement pressure of 50 kPa and axial strain of up to 0.05% as illustrated in Fig. 4. The effective contact modulus and stiffness ratio are determined such that the elastic modulus matches that measured in the laboratory experiments (about 120 MPa). The elastic modulus can be related to the effective contact modulus, E, and the normal-to-shear stiffness ratio, $k = k_n/k_s$, at the contact as follows (Itasca, 2014):

$$k_n := AE/L \tag{1}$$

$$k_s := k_n/k \tag{2}$$

with $A = \pi r^2$

$$r = \begin{Bmatrix} \min(R^{(A)}, R^{(B)}), & \text{ball}-\text{ball} \\ R^{(A)}, & \text{ball}-\text{wall} \end{Bmatrix} \tag{3}$$

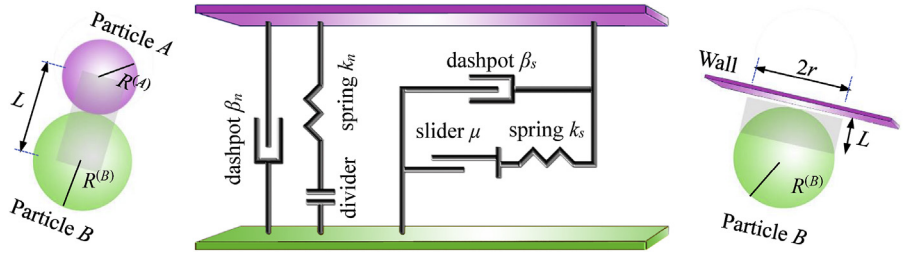

Fig. 2. Micromechanical model and rheology of the particle contact.

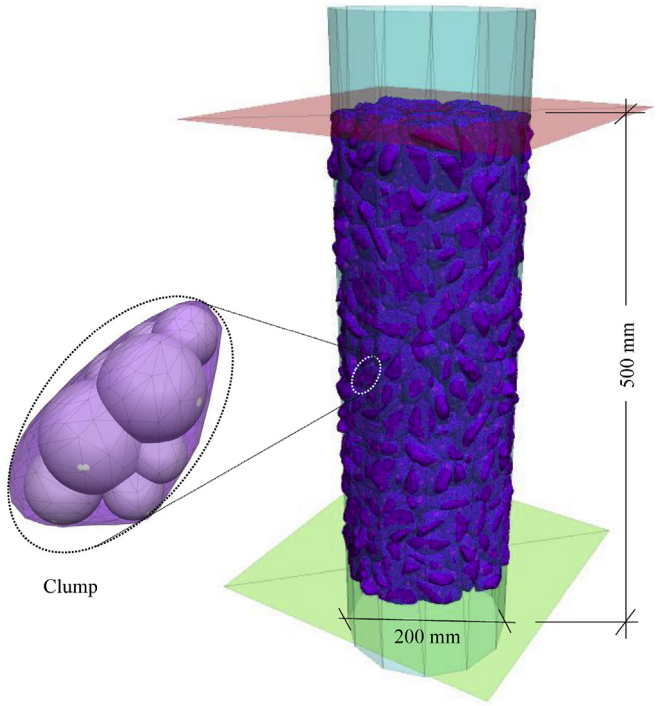

Fig. 3. Simulation of the triaxial compression test.

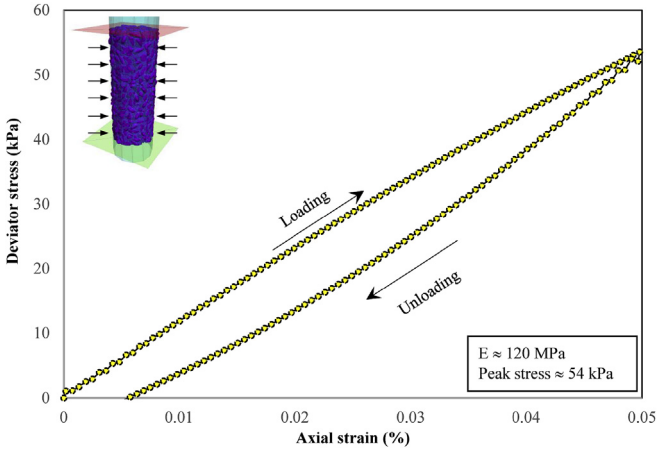

Fig. 4. The loading-unloading portion of the triaxial compression test (confining pressure = 50 kPa).

$$L = \begin{Bmatrix} R^{(A)} + R^{(B)}, & \text{ball–ball} \\ R^{(A)}, & \text{ball–facet} \end{Bmatrix} \tag{4}$$

These two microstructure properties (E and k) were found to be 318 MPa and 1.5, respectively.

2.2. Direct shear tests

The tests were performed using a laboratory shear box measuring 304.8 mm × 304.8 mm × 130.9 mm under three different normal stresses, namely 25, 50 and 75 kPa. The measured friction angle was found to be 53° (Chen et al., 2009). The direct shear tests were numerically modeled considering the dimensions and boundary conditions used in the experiments. Four vertical boundaries (walls) and one horizontal boundary were used to represent the upper and lower parts of the box as shown in Fig. 5. An assembly of spherical particles is generated within the box using a scale factor of 3 without overlapping. After the system is cycled to equilibrium, the spheres were replaced by the previously generated irregular shaped clumps. Normal stress is applied at the top of the sample and is kept constant using a servo-mechanism (Itasca, 2014). The lower part of the box is then moved horizontally at a velocity of 0.1 mm/s, which is consistent with that used in the experiments. It is worth noting that the velocity is applied gradually from 0 to 0.1 mm/s to avoid excessive disturbance of the particle assembly and to reach an evenly shearing stage.

The forces acting on the shear band in both the normal and shear directions (F_N and F_S) were calculated and to determine the equivalent boundary normal σ_n and shear σ_s stresses using the equations below:

$$\sigma_n = \frac{F_N}{L(B - vt)} \tag{5}$$

$$\sigma_s = \frac{F_S}{L(B - vt)} \tag{6}$$

where, L and B are the length and width of the shear box. For a given shear velocity v, and time t, the contact area is $L(B - vt)$. The shear stress-shear displacement relationships for the three performed tests are shown in Fig. 6. The response is characterised by peak shear stresses developing at shear displacements that range from 4 mm to 5 mm depending on the applied normal stress. Residual shear stresses were reached when the shear displacements approached 35 mm. The calculated peak stresses are 36 kPa, 67 kPa and 102 kPa for applied normal stresses of 25, 50, and 75 kPa, respectively. These results are consistent with the measured values in the direct shear tests (Chen et al., 2009). Fig. 7 presents the relationship between normal and shear stresses for both peak and residual values. Results indicated that the peak and residual friction angles of the modeled particles are approximately 53° and 36°, respectively. Based on this analysis, the particle friction coefficient that produce these friction angles is found to be 0.32.

To quantitatively assess the anisotropy features of the modeled material during shear, Fig. 8 shows the contact force network among the distinct particles at shear displacements of 0 mm, 5 mm, and 40 mm, respectively under normal stress of 75 kPa. Forces in the granular assembly are transferred via interconnected network of force chains. The centers of the contacting particles are connected using lines with thicknesses that represent the magnitude of the contact (normal and tangential) forces. At the initial stage (Fig. 8a), contact forces are transmitted mainly in the vertical direction with maximum value of 61 N. With the application of shear displacement, contact forces increased and reached a maximum value of 624 N as peak strength is

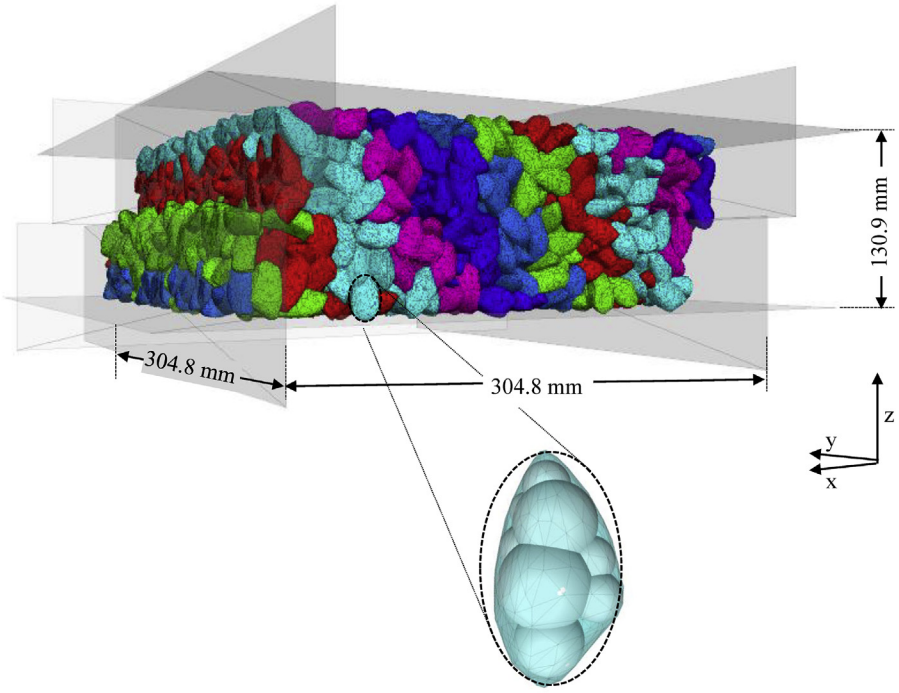

Fig. 5. Modeling the direct shear test at applied shear strain of 8%.

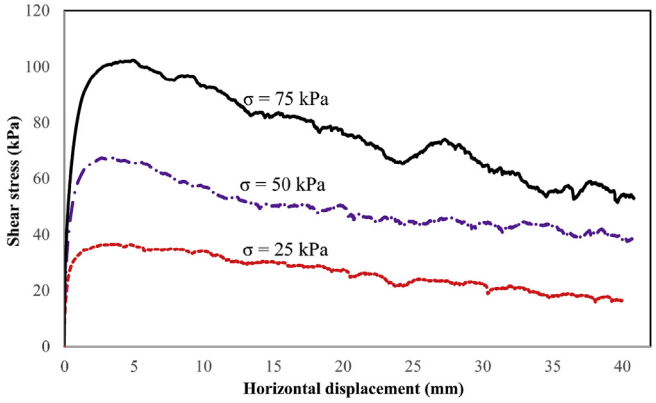

Fig. 6. Shear stress-shear displacement relationship.

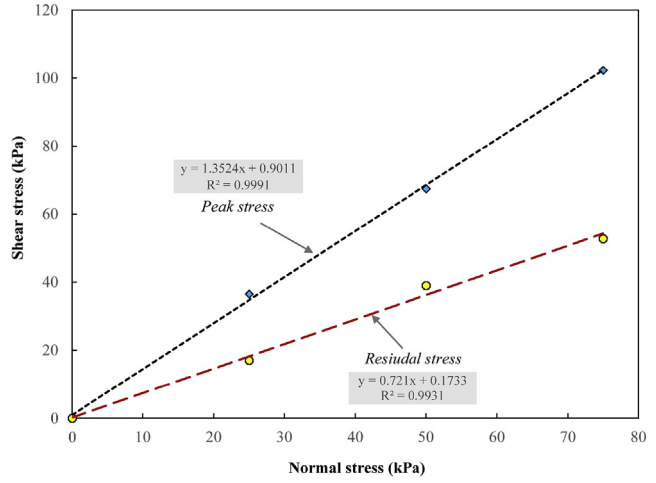

Fig. 7. Peak and residual shear stresses obtained using direct shear test.

reached. At the end of the shearing process (residual state), the maximum contact force decreased to 510 N (Fig. 8c). This is consistent with the decrease in the average number of contacts that the sample experienced at this stage.

To better understand the development of the force chains within the specimen, the contact force distributions are presented using polar histograms as shown in Fig. 8d through 8f. The investigated regions were chosen to allow for the shear bands to be tracked away from the rigid boundaries. The polar histograms were obtained by statistically collecting the contact orientation and distribution of forces at angular interval (bin angle) of 10°. The spatial vectors of the contact orientation and normal and tangential force distribution functions are projected onto the *xoz* plane and the contact normal and shear forces are normalized with respect to the average normal forces over all contacts. Results indicate that contact tangential forces are absent in the sample before shearing owing to the zero interparticle friction used in the generation stage to achieve high relative density. In addition, normal contact forces are uniformly distributed as shown in Fig. 8a. With the increase in shear displacement (Fig. 8b and c), fabric anisotropy and contact tangential forces started to increase resulting in progressive changes in contact orientation from the vertical to the diagonal direction.

Fig. 8d through 8f show the Fourier Series Approximations (FSA) of the normalized contact and force distributions using the dashed lines calculated based on the work of Bathurst and Rothenburg (1990, 1992). The FSA method describes the fabric anisotropy among particles by collecting the contact force information in a zone of interest with a predefined bin angle. The basic idea is that the orientation can be described using a probability density function such that the contact normal distribution function, $E(\theta)$, provides the portion of contact orientations falling within the bin angle. An adequate approximation of the normalized contact orientation distribution can be obtained on the basis of a second Fourier component expressed by equation (7) through (10):

$$E(\theta) = \frac{1}{2\pi}[1 + a_c \cos 2(\theta - \theta_c)] \tag{7}$$

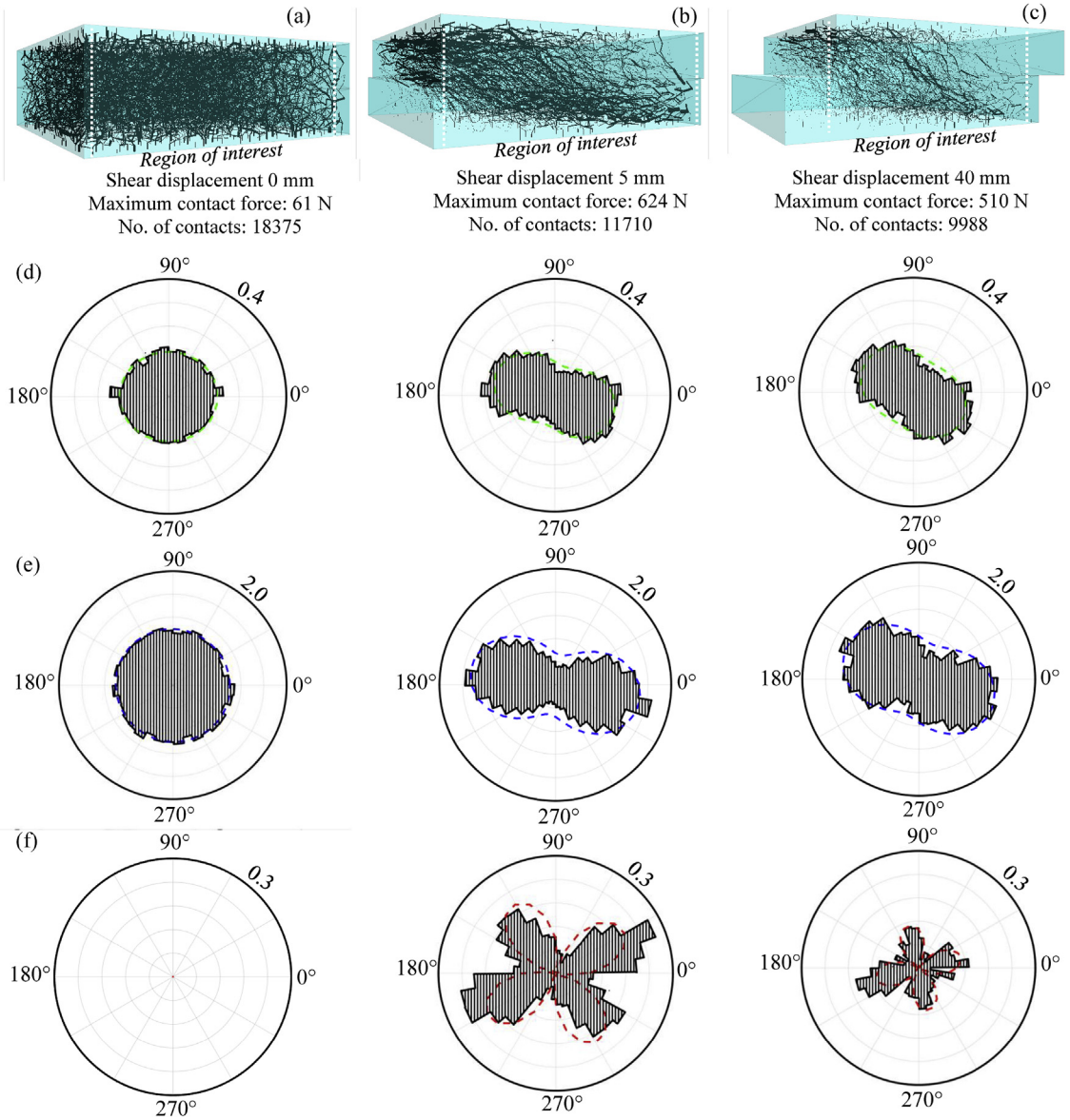

Fig. 8. Distribution and orientation of contact forces: (a) contact force distribution before shearing; (b) contact force distribution at peak state; (c) contact force distribution at residual state; (d) contact normal orientations; (e) contact normal forces; (f) contact shear forces.

$$\overline{f}_0 = \frac{1}{2\pi}\int_0^{2\pi} \overline{f}_n(\theta)d\theta = \frac{1}{N}\sum_{k=1}^{N} f_n^k \tag{8}$$

$$\overline{f}_n(\theta) = \overline{f}_0[1 + a_n \cos 2(\theta - \theta_n)] \tag{9}$$

$$\overline{f}_t(\theta) = -\overline{f}_0 a_t \sin 2(\theta - \theta_t) \tag{10}$$

where $E(\theta)$ represents the contact normal distribution function; $\overline{f}_0$ represents the average normal contact force over all contacts; $\overline{f}_n(\theta)$ and $\overline{f}_t(\theta)$ represent the average normal and tangential force distributions; a_c, a_n and a_t are the second-order coefficients of the contact normal, average normal and tangential contact force anisotropy, respectively; θ_c, θ_n and θ_t represent the corresponding principal directions for the above anisotropy; N represents the number of orientation intervals used in the approximation; and f_n^k represents the contact normal force in each orientation interval.

It is noted that a_c is a deviatoric invariant of a symmetric second-order tensor describing the distribution of contact orientations and θ_c is an eigenvector of this tensor (Rothenburg and Bathurst, 1989). These parameters can be determined using equations (11) and (12) below:

$$\int_0^{2\pi} E(\theta)\cos(2\theta)d\theta = (a_c/2)\cos(2\theta_c) \tag{11}$$

$$\int_0^{2\pi} E(\theta)\sin(2\theta)d\theta = (a_c/2)\sin(2\theta_c) \tag{12}$$

Table 1 shows the coefficients of the Fourier Series Approximation at different shear displacements. The force anisotropies were found to grow distinctly after shearing, and reach theirs maximum at peak state.

Table 1
Coefficients of the fourier series approximation.

Coefficient	Before shear begins	At shear displacement of 5 mm (peak state)	At shear displacement of 40 mm (residual state)
a_c	0.0448	0.3522	0.2433
a_n	0.0145	0.4860	0.3603
a_t	–	0.2047	0.1109
θ_c	3.1215	2.7981	2.5832
θ_n	2.6476	2.9461	2.7537
θ_t	–	1.3513	1.0217

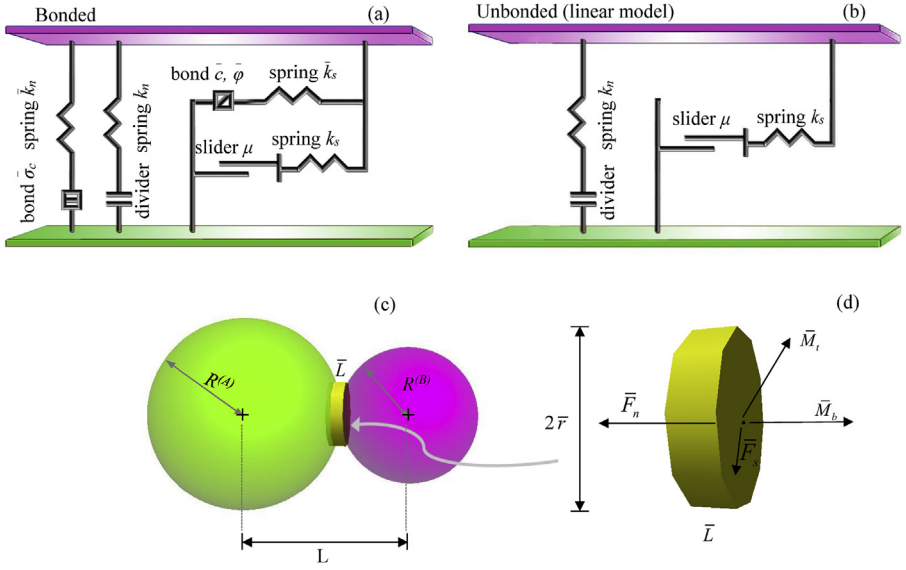

Fig. 9. Rheological components of the linear parallel bond model.

Post peak shear strength was found to decrease as anisotropies of the contact forces started to decrease (Fig. 8d, e and 8f). The results obtained using the FSA method confirms the numerically calculated fabric anisotropy and contact shear stress distribution inside the shear zone.

3. Modeling biaxial geogrid

The geogrid used in this study is modeled as strings of overlapping spherical particles joined by linear parallel bonds that allow for the geometrical and mechanical properties of the biaxial geogrid material to be properly simulated. The rheological model depicted in Fig. 9 shows that the parallel bond consists of two different interfaces: (i) an infinitesimal, linear elastic (no-tension) frictional interface that carries a force; and (ii) a finite-size, linear elastic bonded interface that carries a force and moment (see Fig. 9a). The first interface does not resist relative rotation and slip is accommodated by imposing a Coulomb limit on the shear force. The second interface (parallel bond) resists relative rotation and behaves linearly elastic until the strength limit is exceeded and the bond breaks, making it unbonded (Fig. 9b). The spring element in the parallel bond model is characterised by a bond radius $\bar{r}$ and length $\bar{L}$, as shown in Fig. 9c and d. The microparameters required for the first interface include the effective contact modulus E and normal-to-shear stiffness ratio k, whereas bond effective modulus $\bar{E}$ and bond normal-to-shear stiffness ratio $\bar{k}$ are required for the second interface. The effective contact modulus E can be calculated using equations (1)–(4), whereas the bond effective modulus $\bar{E}$ and bond stiffness ratio $\bar{k}_n/\bar{k}_s$ can be calculated using equations (11a) and (12a) below:

$$\bar{k}_n := \bar{E}/L \tag{11a}$$

$$\bar{k}_s := \bar{k}_n/\bar{k} \tag{12a}$$

The length L can be obtained using equation (4).

The maximum normal and shear stresses at the parallel-bond periphery can be computed as:

$$\sigma_{\max} = \frac{\bar{F}_n}{A} + \frac{\bar{M}_b \bar{R}}{I} \tag{13}$$

$$\tau_{\max} = \frac{\bar{F}_s}{A} + \frac{\bar{M}_t \bar{R}}{J} \tag{14}$$

where $\bar{F}_n$ and $\bar{F}_s$ are the normal and shear stresses of the parallel bond, A is the cross-sectional area, I and J are the moment of inertia and polar moment of inertia of the cross-section, respectively. $\bar{M}_t$ and $\bar{M}_b$ are the twisting and bending components of the moment. The parallel bond is assumed to behave linearly elastic until the allowable stresses are exceeded and the parallel bond breaks resulting in geogrid cracking and failure.

3.1. Geogrid model calibration

The micromechanical parameters needed for modeling the biaxial geogrid are calibrated using index tests as depicted in Fig. 10. A series of tensile tests was performed to measure the load-displacement response of the biaxial geogrid samples (Hussein and Meguid, 2016). The tests were conducted according to the ASTM standard D6637-11 (2011) on multi-rib polypropylene (PP) geogrid specimens in both the machine (MD) and the cross machine (XMD) directions. The geogrid model consists of three main elements: longitudinal ribs, transverse bars and connecting junctions. Each longitudinal rib and transverse bar consists of 20 and 16 overlapping spherical particles, respectively. The diameter of these particles is 4 mm, which results in a uniform thickness for both the transverse and longitudinal members. To capture the junction rigidity, each junction was formed using eight particles arranged as shown in Fig. 10.

The uniaxial tensile tests are numerically simulated using the created geogrid model following the procedure and loading rate used in the experiments (10% strain/min). Matching the loading rate is particularly important for PP geogrids as it can have an effect on the tensile response of the geogrid material (Shinoda and Bathurst, 2004; Ezzein et al., 2015; Wang et al., 2016). The microparameters, including the effective contact modulus, E, stiffness ratio, k_n/k_s, friction coefficient, μ, bond strength, bond effective modulus, $\bar{E}$ are adjusted such that the calculated response satisfies to a large extent that measured in the experiment (see Fig. 11). It is important to note that the parallel bond model uses elastic springs at the particle contacts and, therefore, the visco-elastic behaviour of the geogrid is not captured in the analysis. This simplified approach allows for the geogrid parameters to be calibrated within the small strain range and is widely accepted by researchers (e.g. McDowell et al., 2006; Ngo et al., 2014; Wang et al., 2016).

Flexural rigidity is recognised as one of the important attributes of geogrids in reinforced-soils. The bonded particles used to model the geogrid can result in high bending stiffness and, therefore, additional model validation for flexural bending is needed. This can be achieved using self-weight cantilever tests (Gu et al., 2017b). A geogrid sample 518 mm in length and 83 mm in width was used in the bending tests, as

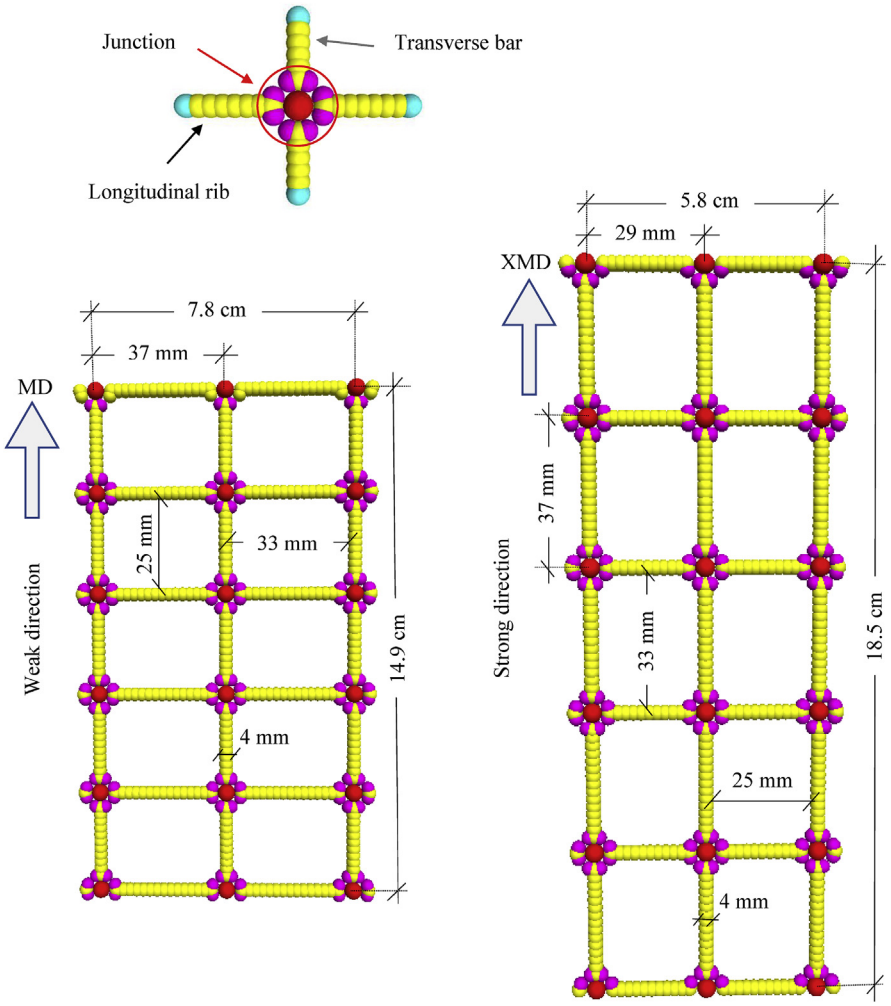

Fig. 10. Discrete element modeling of the multi-rib tensile test.

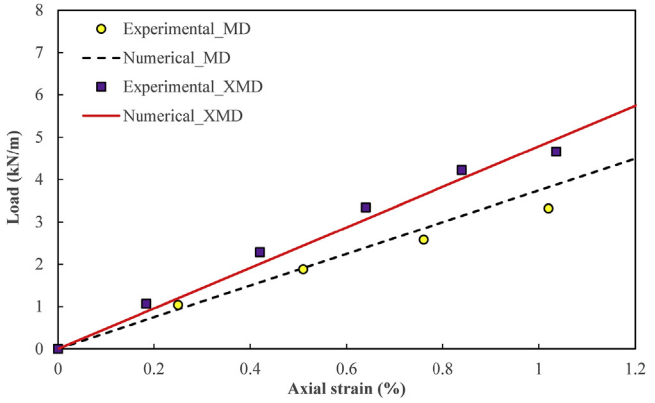

Fig. 11. Model performance: calculated versus measured responses of the geogrid in both the MD and XMD.

depicted in Fig. 12, and the vertical displacement was repeatedly measured when equilibrium condition was reached. The measured results (summarized in Fig. 12c) show that the average vertical displacement at the free end is 322 mm. The bending test was then simulated using the bonded model described above (Fig. 12b) and the model parameters given in Table 2. Particles at the right boundary were fixed in three directions allowing the particles to freely move under gravity. The calculated vertical displacement was found to be 314 mm. This provides a qualitative validation of the flexural rigidity of the model, which is consistent with the findings reported by Chen et al. (2014) and Gu et al., 2017a.

4. Modeling the geogrid-soil system

The purpose of this section is to examine the role of particle shape and geogrid model developed in the previous sections on the response of a typical soil-structure interaction system. To achieve this objective, the experimental results reported by Chen et al. (2009) are modeled using the proposed discrete element approach. The setup consists of a rigid box 1.5 m in length, 0.91 m in width and 0.91 m in height that hosts the crushed limestone backfill material. Footing pressure was applied using a steel plate that measures 152 mm × 152 mm. Rough footing surface was achieved by cementing a thin layer of fine limestone particles onto the base of the footing. The testing procedure was performed based on the ASTM D 1196-93 standard (ASTM, 1997), where small load increments were applied to allow for the load-deflection response to be properly tracked. A loading rate of 0.001 mm/s was used in the analysis to insure a quasi-static response and allow the soil-geogrid system to adjust as the load is applied. A comparison is made between the calculated and measured responses for the cases of unreinforced and reinforced backfill generated using the irregular shaped clumps as well as the conventional spherical discrete element particles. Although the load-displacement response of the geogrid is known to be rate-dependent (Ezzein et al., 2015), the model used in the discrete element analysis is rate-independent. This was deemed acceptable for the purpose of this study as the emphasis is placed on studying

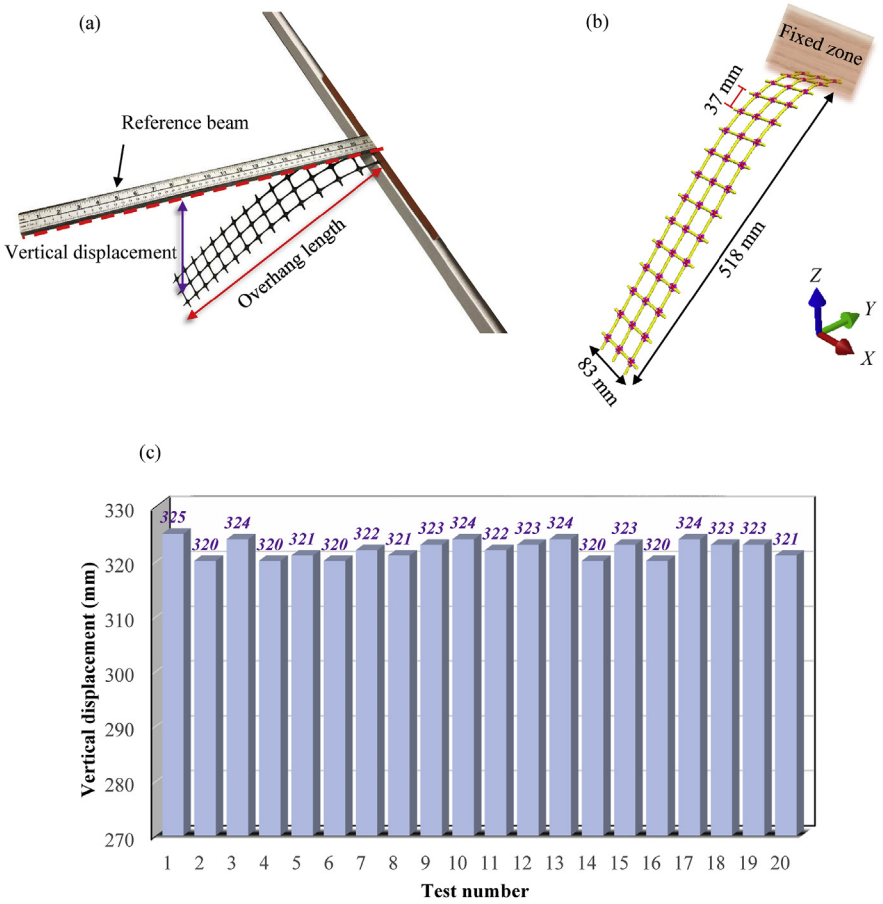

Fig. 12. Geogrid flexural bending test: (a) physical experiment; (b) DEM model; (c) vertical displacements measured in the experiments.

Table 2
Micromechanical parameters used for the PP geogrid model.

Parameter	Assigned value
Particle density	900
Effective contact modulus (MPa)	0.1
Normal-to-shear stiffness ratio (*kn/ks*)	1.5
Bond effective modulus (MPa)	900
Bond normal-to-shear Stiffness ratio ($\bar{k}n/\bar{k}s$)	10^4
Parallel bond tensile strength (MPa)	100
Parallel bond cohesion (MPa)	100
Parallel bond friction angle (Degree)	0
Parallel radius multiplier (−)	1.0

the effect of particle shape on the response of the reinforced system.

Considering the twofold symmetry of the problem domain, only one-quarter of the geometry is modeled with symmetric boundary conditions as illustrated in Fig. 13. The interior sides of the generated walls were set to be frictionless to simulate the smooth surfaces in contact with the backfill material (Tran et al., 2013; Tran et al., 2014a; 2014b; Ahmed et al., 2015). To keep the computational cost manageable, the presence of fines and small particles in the backfill is not considered in the analysis. Instead, a simplified approach that involves uniform size clumps of random orientation is used in this study to represent the crushed limestone (Coetzee, 2017). A layer of spherical particles 22.65 mm in diameter (d_{50} = 5.66 with a scale factor of 4) is first generated randomly at the bottom of the box. A rigid platen is lowered to compress the particles until the porosity of the layer reaches a target value (see Fig. 13). This approach, termed the under-compaction method (UCM), was developed by Jiang et al. (2003). Each spherical particle is then replaced by a clump-shaped particle. The first layer is cycled again to equilibrium to reduce the high contact forces produced by particle overlapping due to the replacement process (Lu and Mcdowell, 2006). During this process, both the acceleration and interparticle friction coefficient are set to zero. The process is repeated for the overlying layers until the backfill height reaches the level of the geogrid layer. Two isolated walls were introduced immediately above and below the location of the geogrid sheet. The geogrid is then generated in the space enclosed by the walls and allowed to come in contact with the particles following the removal of the temporary walls.

It should be noted that the biaxial geogrid used in the experiments is the same as that described in Fig. 10 and the analysis is performed using different number of geogrid layers maintaining a separation distance of 50 mm between consecutive layers as well as between the first layer and the soil surface. It is worth noting that although the ratio between the modeled particle size and the separation distance between the geogrid layers may not reflect the ratio used in the experiments, the model is considered appropriate for the purpose of understanding the interaction between the geogrid reinforcement and the granular material.

The compaction of the system is achieved by applying surface pressure to the frictionless particles using a servo-mechanism to ensure uniform initial pressure across the created system. The interparticle friction is then turned on and the system is cycled to equilibrium. The rigid footing is simulated using a small wall 76 mm × 76 mm placed at the top of the compacted backfill and the load is applied incrementally to allow for the response of the system to be recorded for both the unreinforced and the reinforced cases. It is worthwhile noting that the loading rate that is slow enough to insure a quasi-static response.

5. Results and discussion

In this section, the effect of introducing one, two and three geogrid

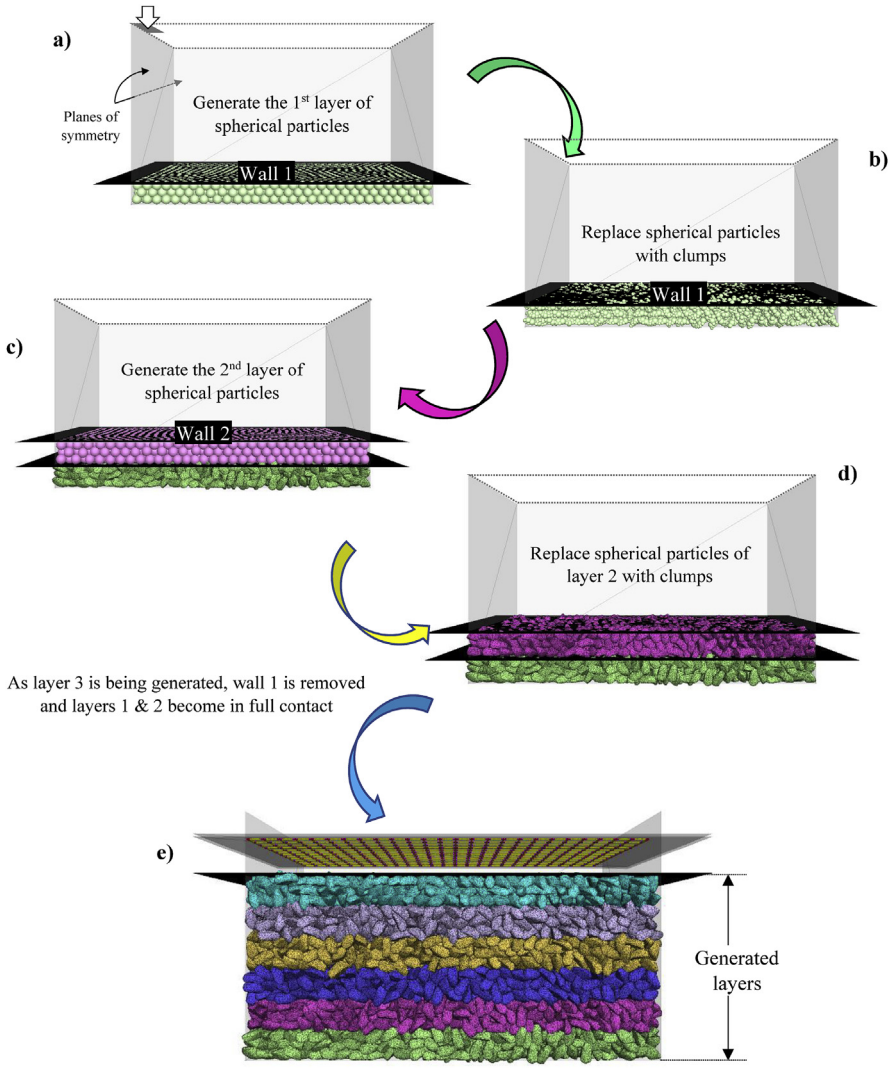

Fig. 13. Schematic showing the generation process of the reinforced system using the undercompaction method.

reinforcement sheets into the crushed limestone is examined and compared with the unreinforced case. Emphasis is placed on the role of particle shape on the response of the reinforced system.

5.1. Validation of the numerical model

Particle shape plays a key role in the behaviour of angular stones (Chen et al., 2014). It influences not only the physical state of the assembly (grain structure and porosity), but also particle-particle interaction, such as interparticle friction, contact force and coordination number. To validate the numerical model, the analysis is performed using both spherical particles and irregular shaped clumps and the results are compared with the experimental data. Fig. 14 shows the relationship between the equivalent footing pressure (calculated numerically) and the vertical settlement for the four investigated cases: unreinforced ($N = 0$) and reinforced using one ($N = 1$), two ($N = 2$) and three geogrid layers ($N = 3$). For the unreinforced case, excessive settlement started to develop at applied footing pressure of about 5 MPa as shown in Fig. 14a. Modeling the crushed limestone using spherical particles generally produced a softer response with more settlement at the same applied pressure. The irregular shaped clumps were found to replicate the correct stiffness and vertical displacement of the footing up to applied pressure of about 5 MPa. Similar behaviour is found for the three reinforced cases (Fig. 14b through 14d) where the model built using clump particles was able to capture the correct response of the geogrid-reinforced system for the entire range of loading. Whereas, spherical particles consistently produced a softer response and unrealistic displacements when compared with the measured values. It is worth noting that for both the unreinforced and reinforced cases, the models slightly underestimated the settlement of the footing as failure is approached. This can be explained by the fact that the used particle models do not allow for the additional settlement resulting from the possible particle crushing to be captured under high loading. It influences not only the physical state of the assembly (grain structure and porosity), but also the particle interaction (interparticle friction, contact force and coordination number).

Further discussion related to the effect of introducing geogrid reinforcement in enhancing the strength of granular material is made in the section below.

5.2. Particle resistance to rotation

Particle resistance to rotation is known to develop in irregular shaped particles and contribute to enhancing the shear strength and dilatancy behaviour of granular assembly. For reinforced material, particle resistance to rotation is expected to increase due to the presence of the geogrid structure. Fig. 15 shows the rotations of the clumps surrounding the geogrid reinforcement for the three investigated cases ($N = 1$, 2 and 3). The rotations are represented by colour coded circles such that the size of each circle is proportional to the magnitude of

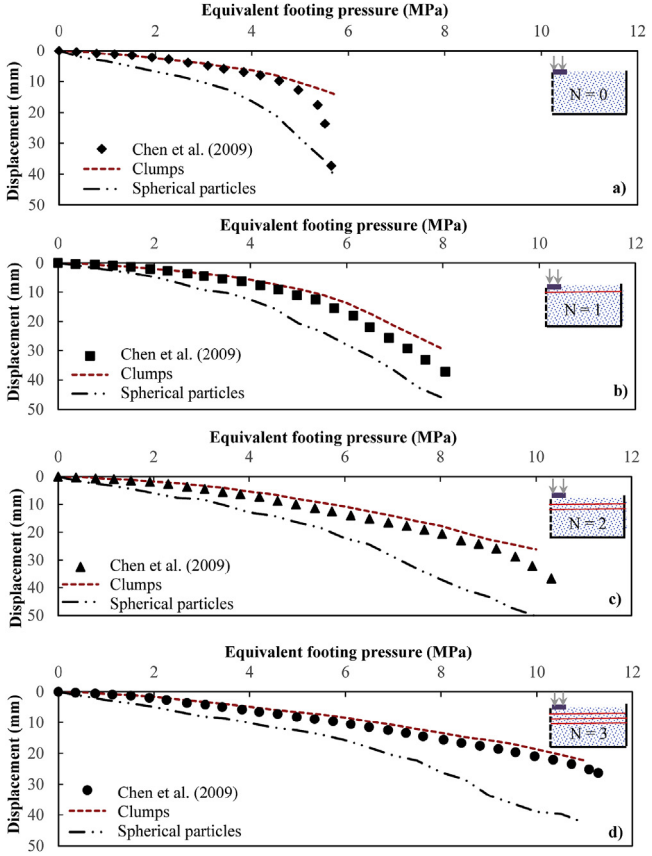

Fig. 14. Load-displacement relationships for: a) unreinforced; b) N = 1; c) N = 2; d) N = 3.

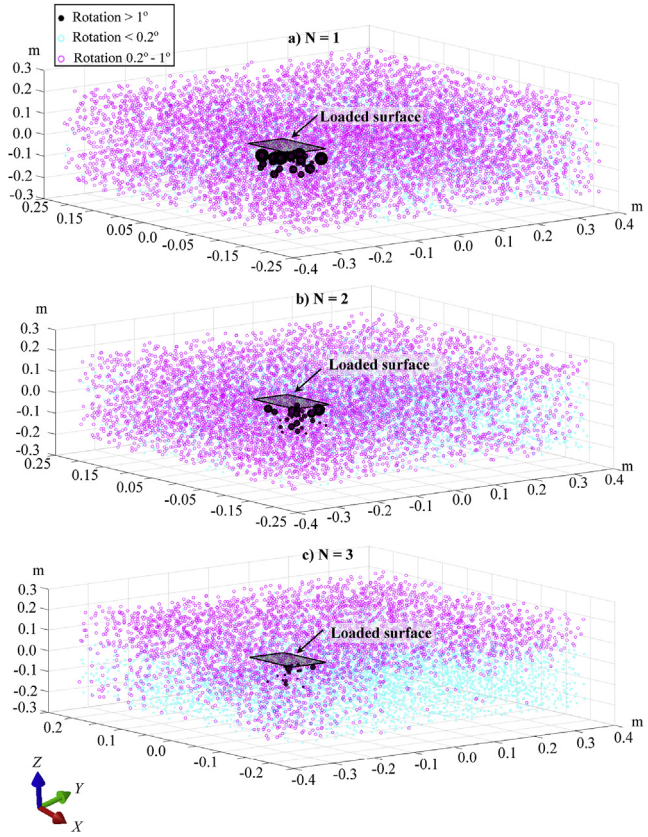

Fig. 15. Rotations of the clumps at footing load of 6 MPa: for a) N = 1; b) N = 2; c) N = 3.

particle rotation. The rotations are calculated as the vector sum of the rotations about three mutually orthogonal axes. The equation used are summarized below.

$$[L] = [I][\omega] \tag{15}$$

Where, I is the inertia tensor and ω is the angular velocity, L is angular momentum. Taking the time derivative of equation (9), the Euler equation is obtained:

$$[M] = [L] = [I][\alpha] + [\omega][L] \tag{16}$$

Where, α is the angular acceleration. I, α, and M are expressed by:

$$[I] = \begin{bmatrix} I_{11} & -I_{12} & -I_{13} \\ -I_{21} & I_{22} & -I_{23} \\ -I_{31} & -I_{32} & I_{33} \end{bmatrix} \tag{17}$$

$$\alpha = \begin{bmatrix} \alpha_1 \\ \alpha_2 \\ \alpha_3 \end{bmatrix} = \begin{bmatrix} \omega_1 \\ \omega_2 \\ \omega_3 \end{bmatrix} \tag{18}$$

$$[M] = \begin{bmatrix} M_1 \\ M_2 \\ M_3 \end{bmatrix} = \begin{bmatrix} I_1\alpha + (I_{33} - I_{22})\omega_3\omega_2 \\ I_2\alpha + (I_{11} - I_{33})\omega_1\omega_3 \\ I_3\alpha + (I_{22} - I_{11})\omega_2\omega_1 \end{bmatrix} \tag{19}$$

Where, M_i represent the resultant moment acting on the distinct particles.

The solid black circles in Fig. 15 indicate rotations of more than 1°, the magenta circles indicate rotations that range between 0.2° and 1°, and the cyan circles illustrate rotations that are smaller than 0.2°. It is found that the number of particles experiencing rotations of more than 1° are concentrated under the footing (Fig. 15a) and decreased with the addition of more geogrid layers (Fig. 15b and c). For $N = 3$, the extent of the magenta circles (rotation from 0.2° to 1°) is significantly smaller compared to the cases of $N = 1$ and 2. This can be explained by the interlocking effect that increased significantly due to the addition of the second and third geogrid layer. In contrast, the extent of the cyan circles (rotation less than 0.2°) increased with the increase in the number of reinforcement layers due to the increase in particle interlocking within the geogrid openings.

The above results confirm that particle resistance to rotation that develop due to the irregular particle shape is significantly enhanced by the introduction of one or more geogrid layers. Undoubtedly, this is a result of the interlocking of the clump particles with the geogrid, which enhances the layer confinement. The confinement effect enabled the geogrid to act as a non-displacement boundary that restrained particle movement and decreased the overall rotation. This interaction is manifested in higher load resistance and smaller displacement under the footing.

5.3. Response of the geogrid

The deformed shapes of the geogrid for a footing pressure of 6 MPa are presented in Fig. 16 for the three cases of $N = 1$, 2 and 3. The displacement generally developed under the loaded area with and decreased with distance from the applied load. For $N = 1$, the maximum displacement reached about 70 mm under the center of the footing (Fig. 16a). When two reinforcing geogrid layers were placed under the footing, the upper layer experienced a maximum displacement of about 50 mm whereas the second layer displaced less than 40 mm (Fig. 16b). For $N = 3$, the upper layer experienced a maximum displacement of about 37 mm (Fig. 16c) whereas, insignificant displacements were calculated for the second and third geogrid layers.

To further illustrate the response of the upper geogrid layer under the applied load, Fig. 17 shows the contours of strains developing in the geogrid for the three investigated cases. The maximum tensile strains in

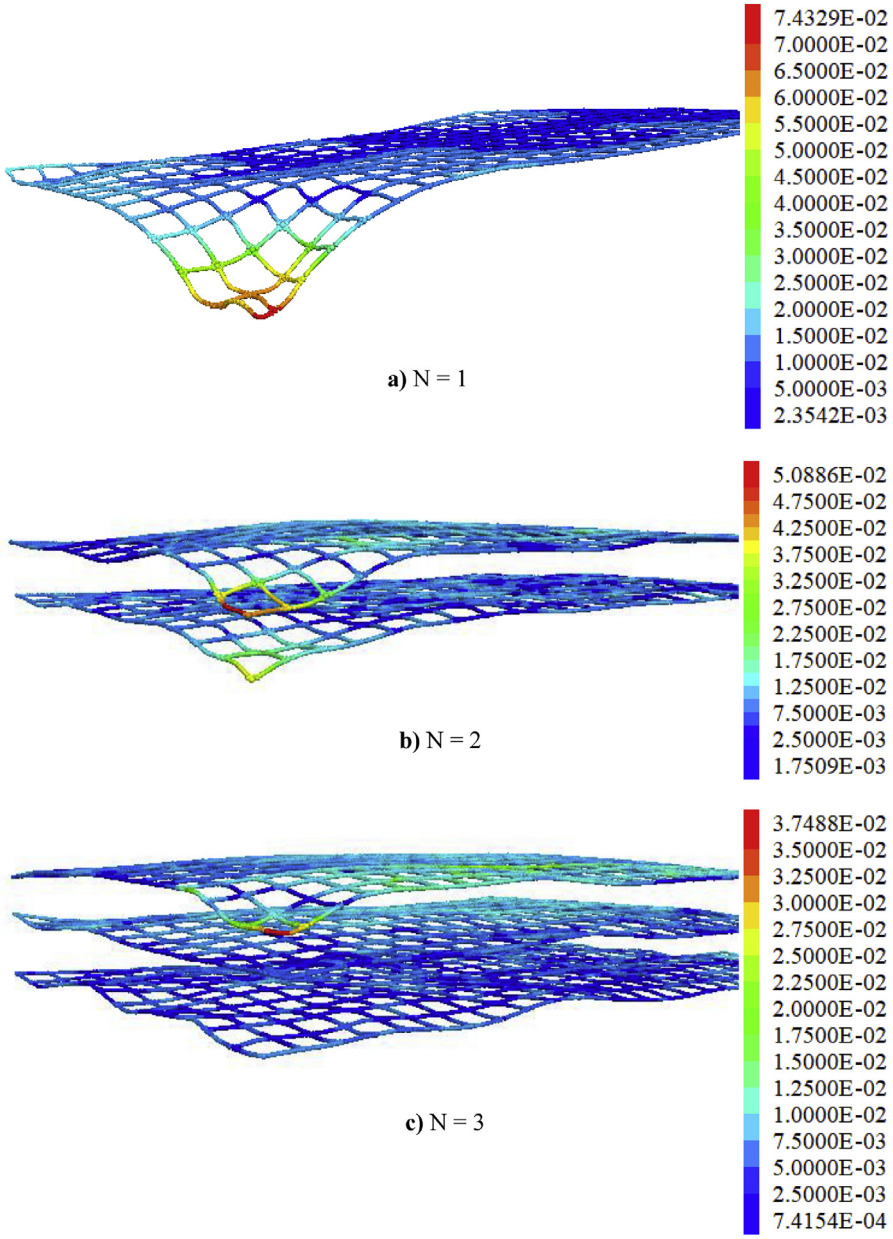

Fig. 16. Geogrid deformation at footing load of 6 MPa for different reinforced systems: a) N = 1; b) N = 2; c) N = 3.

the geogrid are found to be 0.018, 0.015, and 0.011 for the cases of $N = 1$, 2 and 3, respectively. These results are consistent with the increase in additional confinement created by the addition or more geogrid layers. It is worth noting that the uppermost geogrid layer for $N = 2$ and $N = 3$ cases was chosen for the comparison with the case of $N = 1$.

5.4. Contact force network

The contact force networks developing in the granular material due to the applied load are presented in Fig. 18 for the three reinforced cases. To illustrate the effect of modeling the irregular particle shape on the load transfer within the modeled material, the results obtained using spherical particles are also presented in Fig. 18. Each contact force is illustrated by a line connecting the centers of two contacting elements while the width of the line is proportional to the magnitude of the contact force. It is found that, for the three investigated cases, large contact forces generally develop immediately beneath the loaded area. Comparing the left and right columns in Fig. 18, the magnitude of the contact forces when clump particles are used is found to be significantly smaller as compared to the case when the material is modeled using spherical particles. This can be explained by the higher number of contact points in irregular shaped particles resulting in a more homogeneous stress distribution and a denser soil domain.

The above results suggest that modeling angular material using irregular shaped particles is essential to produce realistic responses for both the geogrid and the backfill material. In addition, the geogrid-soil interaction in these cases restricts particle rotation and enhances the shear resistance of the reinforced material.

5.4.1. Limitations

It is recognised that modeling the actual particle size and number of particles used in experiments is not computationally feasible, and therefore scaled particle sizes were used in this study. Although this is not reflective of reality, the results provided sufficient details with respect to the 3D load transfer mechanism between the geogrid and the

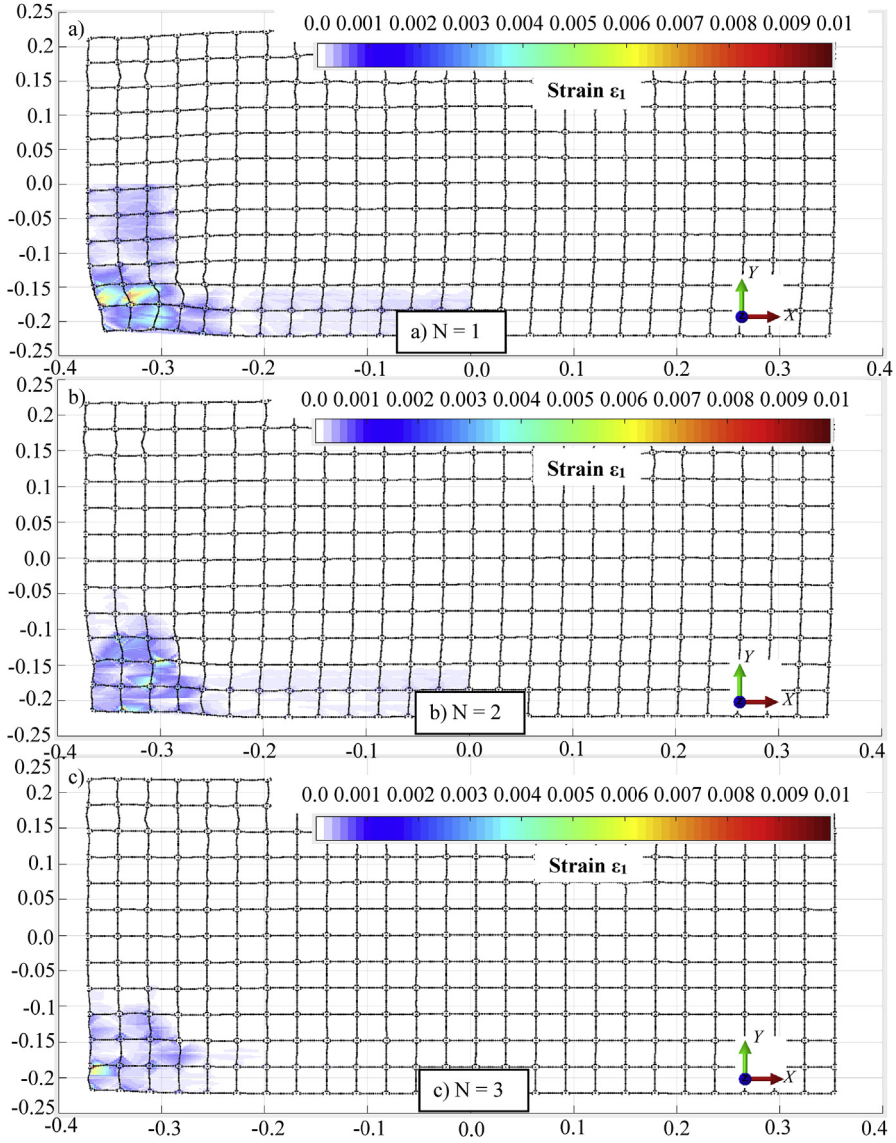

Fig. 17. Strains across the upper geogrid layer at footing load of 6 MPa for: a) N = 1; b) N = 2; c) N = 3.

surrounding backfill material. In addition, the clumps used to model crushed limestones do not fully represent the sharp-edged particles due to the fact that clumps were made of spherical pebbles. Nevertheless, this approach is considered to be reliable enough to investigate the role of particle shape on the response of a soil-geogrid system. Finally, better predictions can be obtained considering the rate-dependent property of the PP geogrid material.

5.4.2. Summary and conclusions

A discrete element procedure for the 3D analysis of unconfined and soil-confined geogrid is developed in this study. To investigate the effect of particle shape on the response of geogrid embedded in crushed limestone material is simulated. The crushed limestone particles are modeled using irregular-shaped clumps. The governing micro-parameters (effective modulus, stiffness ratio, peak and residual friction coefficients) are first calibrated using a series of triaxial-compression and direct shear tests. A numerical model that is capable of simulating the response of the unconfined biaxial geogrid under tensile loading is then developed and validated using index test results. Additionally, simplified flexural bending tests are conducted to determine the flexural rigidity of the geogrid material. In developing this model, the details of the geometrical features are explicitly simulated. A procedure is also developed to simulate a reinforced soil system using the created clump particles and the geogrid sheet. A suitable two-step particle packing using the undercompaction method is adopted to allow for the interlocking effect to be properly captured without changing the initial position and orientation of the particles.

To confirm the validity of the model, the calculated response is compared with existing experimental data for reinforced granular material with one or more geogrid layers under footing pressure. A comparison is made between the results obtained by modeling the granular material as spherical particles and using irregular shaped clumps. Based on the results and discussion presented in the previous section, the following general conclusions can be made:

1 Modeling crushed limestone using spherical-shaped particles resulted in a softer response to loading and higher settlement for both the unreinforced and reinforced cases. This is attributed to the fact that non-spherical particles interlock better with the geogrid resulting in enhanced confinement and improvement in shear strength properties of the granular material. In addition, clumped particles provided additional restraint to rotation due to the increase in packing density.
2 Increasing the number of geogrid layers resulted in a significant

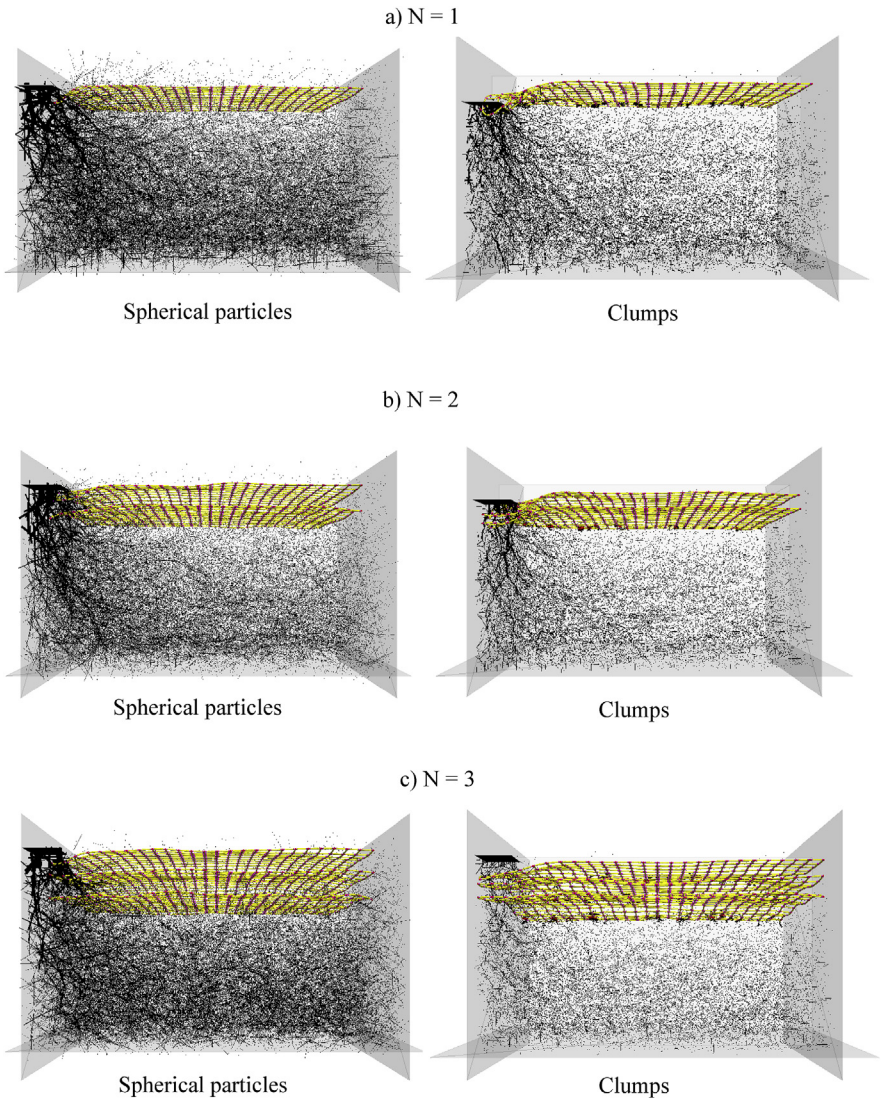

Fig. 18. Contact forces at footing pressure of 6 MPa for: a) N = 1; b) N = 2; N = 3.

increase in the ultimate bearing capacity of the reinforced soil system. When multiple geogrid layers are used, the uppermost layer is found to experience larger deformations and tensile strains compared to the lower layer.

3 The extent and magnitude of the contact forces transmitted to the particle assembly is significantly smaller when clumps are used to represent the irregular shaped particles.

Finally, the proposed discrete element approach for the analysis of reinforced material has been shown to hold much promise in reliably capturing the correct response of a reinforced soil system.

Acknowledgments

This research was supported by a research grant from the Natural Sciences and Engineering Research Council of Canada (RGPIN-2016-05263). The financial support provided by McGill Engineering Doctoral Award (MEDA) to the first author is greatly appreciated. The first author is thankful to Prof. Jiang for his valuable help with the UCM method.

References

Ahmed, M., Tran, V., Meguid, M.A., 2015. On the role of geogrid reinforcement in reducing earth pressures on buried pipes. Soils Found. 55 (3), 588–599.
ASTM, 1997. Standard Test Method for Non Repetitive Static Plate Load Tests of Soils and Flexible Pavement Components, for Use in Evaluation and Design of Airport and Highway Pavements. pp. 112–113.
ASTM, 2011. Standard Test Method for Determining Tensile Properties of Geogrids by the Single or Multi-rib Tensile Method. D6637/D6637M–15, West Conshohocken, PA.
Bathurst, R.J., Ezzein, F.M., 2015. Geogrid and soil displacement observations during pullout using a transparent granular soil. Geotech. Test J. 38 (5), 673–685.
Bathurst, R.J., Ezzein, F.M., 2016. Geogrid pullout load-strain behaviour and modelling using a transparent granular soil. Geosynth. Int. 23 (4), 271–286.
Bathurst, R.J., Ezzein, F.M., 2017. Insights into geogrid-soil interaction using a transparent granular soil. Géotech. Lett. 7, 1–5.
Bathurst, R.J., Rothenburg, L., 1990. Observation on stress-force-fabric relationships in idealized granular materials. Mech. Mater. 9, 65–80.
Bathurst, R.J., Rothenburg, L., 1992. Investigation of micromechanical features of idealized granular assemblies using DEM. Eng. Comput. 9 (2), 199–210.
Cardile, G., Gioffrè, D., Moraci, N., Calvarano, L.S., 2017. Modelling interference between the geogrid bearing members under pullout loading conditions. Geotext. Geomembranes 45 (3), 169–177.
Chen, C., McDowell, G., Thom, N.H., 2012. Discrete element modelling of cyclic loads of geogrid-reinforced ballast under confined and unconfined conditions. Geotext. Geomembranes 35, 76–86.
Chen, C., McDowell, G., 2013. A study of geogrid-reinforced ballast using laboratory pullout tests and discrete element modelling. Geomechanics Geoengin.: Int. J. 8 (4), 244–253.
Chen, C., McDowell, G., Thom, N.H., 2014. Investigating geogrid-reinforced ballast: experimental pull-out tests and discrete element modeling. Soils Found. 54 (1), 1–11.
Chen, Q., Abu-Farsakh, M., Sharma, R., 2009. Experimental and analytical studies of reinforced crushed limestone. Geotext. Geomembranes 27 (5), 357–367.
Coetzee, C.J., 2017. Review: calibration of the discrete element method. Powder Technol. 310, 104–142.

Cundall, P.A., Strack, O.D.L., 1979. A discrete numerical model for granular assemblies. Geotechnique 29 (1), 47–65.
Demir, A., Laman, M., Yildiz, A., Ornek, M., 2013. Large scale field tests on geogrid reinforced granular fill underlain by soft clay. Geotext. Geomembranes 38, 1–15.
Esmaeili, M., Zakeri, J.A., Babaei, M., 2017. Laboratory and field investigation of the effect of geogrid-reinforced ballast on railway track lateral resistance. Geotext. Geomembranes 45 (2), 23–33.
Ezzein, F.M., Bathurst, R.J., 2014. A new approach to evaluate soil-geosynthetic interaction using a novel pullout test apparatus and transparent granular soil. Geotext. Geomembranes 42 (3), 246–255.
Ezzein, F.M., Bathurst, R.J., Kongkitkul, W., 2015. Nonlinear load–strain modeling of polypropylene geogrids during constant rate-of-strain loading. Polym. Eng. Sci. 55 (7), 1617–1627.
Gao, G., Meguid, M.A., 2018a. On the role of sphericity of falling rock clusters- Insights from experimental and numerical investigations. Landslides 15 (2), 219–232.
Gao, G., Meguid, M.A., 2018b. Modeling the impact of a falling rock cluster on rigid structures. ASCE. Int. J. Geomechanics 18 (2), 1–15.
Gu, M., Han, J., Zhao, M., 2017a. Three-dimensional discrete-element method analysis of stresses and deformations of a single geogrid-encased stone column. Int. J. GeoMech. 17 (9), 1–14.
Gu, M., Han, J., Zhao, M., 2017b. Three-dimensional DEM analysis of single geogrid-encased stone columns under unconfined compression: a parametric study. Acta Geotechnica 12 (3), 559–572.
Hussein, M.G., Meguid, M.A., 2016. A three-dimensional finite element approach for modeling biaxial geogrid with application to geogrid-reinforced soils. Geotext. Geomembranes 44 (3), 295–307.
Indraratna, B., Ngo, N.T., Rujikiatkamjorn, C., Vinod, J., 2014. Behavior of fresh and fouled railway ballast subjected to direct shear testing: discrete element simulation. Int. J. GeoMech. 34–44. http://dx.doi.org/10.1061/(ASCE)GM.1943-5622.0000264.
Itasca, 2014. Particle Flow Code in Three Dimensions (PFC3D), Minneapolis.
Jiang, M.J., Konrad, J.M., Leroueil, S., 2003. An efficient technique for generating homogeneous specimens for DEM studies. Comput. Geotech. 30 (7), 579–597.
Jiang, M.J., Li, T., Shen, Z., 2016. Fabric rates of elliptical particle assembly in monotonic and cyclic simple shear tests: a numerical study. Granul. Matter 18 (54), 1–14.
Kumar, J., Sahoo, J.P., 2013. Bearing capacity of strip foundations reinforced with geogrid sheets by using upper bound finite-element limit analysis. Int. J. Numer. Anal. Meth. GeoMech. 37 (18), 3258–3277.
Lai, Z., Chen, Q., 2017. Characterization and discrete element simulation of grading and shape-dependent behavior of JSC-1A Martian regolith simulant. Granul. Matter 19 (69). https://doi.org/10.1007/s10035-017-0754-1.
Lai, H.J., Zheng, J.J., Zhang, J., Zhang, R.J., Cui, L., 2014. DEM analysis of "soil"-arching within geogrid-reinforced and unreinforced pile-supported embankments. Comput. Geotech. 61, 13–23.
Li, F.-L., Peng, F.-L., Tan, Y., Kongkitkul, W., Siddiquee, M.S.A., 2012. FE simulation of viscous behavior of geogrid-reinforced sand under laboratory-scale plane-strain-compression testing. Geotext. Geomembranes 31, 72–80.
Lin, Y.L., Zhang, M.X., Javadi, A.A., Lu, Y., Zhang, S.L., 2013. Experimental and DEM simulation of sandy soil reinforced with H–V inclusions in plane strain tests. Geosynth. Int. 20 (3), 162–173.
Ling, H.I., Liu, H., 2009. Deformation analysis of reinforced soil retaining walls – simplistic versus sophisticated finite element analyses. Acta Geotechnica 4, 203–213.
Lu, M., Mcdowell, G.R., 2006. Discrete element modelling of ballast abrasion. Geotechnique 56, 651–655.
McDowell, G.R., Harireche, O., Konietzky, H., Brown, S.F., Thom, N.H., 2006. Discrete element modelling of geogrid-reinforced aggregates. Geotechnical Engineering – ICE 159 (1), 35–48.
Masson, S., Martinez, J., 2001. Micromechanical analysis of the shear behavior of a granular material. J. Eng. Mech. 127, 1007–1016.
Miao, C., Zheng, J., Zhang, R., Cui, L., 2017. DEM modeling of pullout behavior of geogrid reinforced ballast: the effect of particle shape. Comput. Geotech. 81, 249–261.
Moraci, N., Recalcati, P., 2006. Factors affecting the pullout behaviour of extruded geogrids embedded in a compacted granular soil. Geotext. Geomembranes 24 (4), 220–242.
Mousavi, S.H., Mohammed, A.G., Borden, R.H., 2017. Optimum location of geogrid reinforcement in unpaved road. Can. Geotech. J. 54 (7), 1047–1054.
Ngo, N.T., Indraratna, B., Rujikiatkamjorn, C., 2014. DEM simulation of the behaviour of geogrid stabilised ballast fouled with coal. Comput. Geotech. 55, 224–231.
Ngo, N.T., Indraratna, B., Rujikiatkamjorn, C., 2017. A study of the geogrid–subballast interface via experimental evaluation and discrete element modelling. Granul. Matter. http://dx.doi.org/10.1007/s10035-017-0743-4.
Palmeira, E.M., Milligan, G.W.E., 1989. Scale and other factors affecting the results of pull-out tests of girds buried in sand. Geotechnique 39 (3), 511–524.
Rothenburg, L., Bathurst, R.J., 1989. Analytical study of induced anisotropy in idealized granular materials. Géotechnique 39 (4), 601–614.
Rowe, R.K., Liu, K.W., 2015. Three-dimensional finite element modelling of a full-scale geosynthetic-reinforced, pile-supported embankment. Can. Geotech. J. 52 (12), 2041–2054.
Saha Roy, S.M., Deb, K., 2017. Effects of aspect ratio of footings on bearing capacity for geogrid-reinforced sand over soft soil. Geosynth. Int. 24 (4), 362–382.
Shen, W.G., Zhao, T., Crosta, G.B., Dai, F., 2017. Analysis of impact induced rock fragmentation using a discrete element approach. Int. J. Rock Mech. Min. Sci. 98, 33–38.
Shin, E.C., Das, B.M., 2000. Experimental study of bearing capacity of a strip foundation on geogrid- reinforced sand. Geosynth. Int. 7 (1) 59–7.
Shinoda, M., Bathurst, R.J., 2004. Lateral and axial deformation of PP, HDPE and PET geogrids under tensile load. Geotext. Geomembranes 22 (4), 205–222.
Sitharam, T.G., Sireesh, S., 2004. Model studies of embedded circular footing on geogrid-reinforced sand beds. Ground Improv. 8 (2), 69–75.
Stahl, M., Konietzky, H., 2011. Discrete element simulation of ballast and gravel under special consideration of grain-shape, grain-size and relative density. Granul. Matter 13 (4), 417–428.
Stahl, M., Konietzky, H., Kamp, L., Jas, H., 2014. Discrete element simulation of geogrid-stabilised soil. Acta Geotechnica 9 (6), 1073–1084.
Tran, V.D.H., Meguid, M.A., Chouinard, L.E., 2013. A finite-discrete element framework for the 3D modeling of geogrid-soil interaction under pullout loading conditions. Geotext. Geomembranes 37, 1–9.
Tran, V., Meguid, M.A., Chouinard, L.E., 2014a. Three-dimensional analysis of geogrid-reinforced soil using a finite-discrete element framework. ASCE. Int. J. Geomechanics 15 (4), 1–19.
Tran, V.D.H., Meguid, M.A., Chouinard, L.E., 2014b. Discrete element and experimental investigations of the earth pressure distribution on cylindrical shafts. ASCE. Int. J. Geomechanics 14 (1), 80–91.
Wang, Z., Jacobs, F., Ziegler, M., 2016. Experimental and DEM investigation of geogrid-soil interaction under pullout loads. Geotext. Geomembranes 44 (3), 230–246.
Zhuang, Y., Wang, K.Y., 2016. Finite-Element analysis on the effect of subsoil in reinforced piled embankments and comparison with theoretical method predictions. Int. J. GeoMech. http://dx.doi.org/10.1061/(ASCE)GM.1943-5622.0000628.